OPEN ACCESS
IOP Publishing | IMMT
International Journal of Extreme Manufacturing
Int. J. Extrem. Manuf. 7 (2025) 025504 (13pp)
https://doi.org/10.1088/2631-7990/ad92cb

3D-programmable streamline guided orientation in composite materials for targeted heat dissipation

Xinfeng Zhang[1], Xuan Yang[1], Yiwen Fan[1], Run Hu[1], Bin Xie[2,*] and Xiaobing Luo[1,*]

[1] State Key Laboratory of Combustion, School of Energy and Power Engineering, Huazhong University of Science and Technology, Wuhan 430074, People's Republic of China
[2] School of Mechanical Science and Engineering, Huazhong University of Science and Technology, Wuhan 430074, People's Republic of China

E-mail: binxie@hust.edu.cn and luoxb@hust.edu.cn

Received 5 February 2024, revised 30 August 2024
Accepted for publication 5 September 2024
Published 2 December 2024

Abstract

Filler-reinforced polymer composites demonstrate pervasive applications due to their strengthened performances, multi-degree tunability, and ease of manufacturing. In thermal management field, polymer composites reinforced with thermally conductive fillers are widely adopted as thermal interface materials (TIMs). However, the three dimensional (3D)-stacked heterogenous integration of electronic devices has posed the problem that high-density heat sources are spatially distributed in the package. This situation puts forward new requirements for TIMs, where efficient heat dissipation channels must be established according to the specific distribution of discrete heat sources. To address this challenge, a 3D printing-assisted streamline orientation (3D-PSO) method was proposed to fabricate composite thermal materials with 3D programmable microstructures and orientations of fillers, which combines the shape-design capability of 3D printing and oriented control ability of fluid. The mechanism of fluid-based filler orientation control along streamlines was revealed by mechanical analysis of fillers in matrix. Thanks to the designed heat dissipation channels, composites showed better thermal and mechanical properties in comparison to random composites. Specifically, the thermal conductivity of 3D mesh-shape polydimethylsiloxane/liquid metal (PDMS/LM) composite was 5.8 times that of random PDMS/LM composite under filler loading of 34.8 vol%. The thermal conductivity enhancement efficiency of 3D mesh-shape PDMS/carbon fibers composite reached 101.05% under filler loading of 5.2 vol%. In the heat dissipation application of 3D-stacked chips, the highest chip temperature with 3D-PSO composite was 42.14 °C lower than that with random composites. This is mainly attributed to the locally aggregated and oriented fillers' microstructure in fluid channels, which contributes to thermal percolation phenomena. The 3D-PSO method exhibits excellent programmable design capabilities to adopt versatile distributions of heat sources, paving a new way to solve the complicated heat dissipation issue in 3D-stacked chips integration application.

* Authors to whom any correspondence should be addressed.

2631-7990/25/025504+13$33.00

Supplementary material for this article is available online

Keywords: thermal materials, 3D heat dissipation channels, 3D-stacked chips, heat dissipation, 3D printing, orientation control

1. Introduction

Composite functional materials (CFMs) have been adopted in a wide range of fields owing to their diversity, adaptability, and low cost. Among them, filler-reinforced polymer composite is the most frequently adopted CFMs since their properties can be easily engineered to adapt to various applications [1–5]. In electronic devices, thermal interface materials (TIMs) with high thermal conductivity are indispensable for filling the gaps between bonding and packaging interfaces to ensure the performance and reliability of the devices [6, 7]. Filler-reinforced polymer composites exhibit excellent potential as TIMs owing to their superior flexibility, excellent durability and high adjustability. However, low thermal conductivity of polymer remains an obstacle to its application. Therefore, a variety of thermal conductive fillers are screened out and filled into polymer according to thermal conductivity, electrical conductivity, shape (spheroidal, rod-like, sheet-like, etc) and size (from nanoscale to microscale). Typically, thermally conductive fillers include metal or metal oxides (e.g. Al, Cu, CuO) [8–10], ceramics (e.g. BN, AlN) [11–15], carbon-based fillers (e.g. graphene, carbon fibers) [16], etc. Randomly filling the fillers into polymer matrix is insufficient for improving their thermal performance due to separation of fillers and the interfaces between fillers and matrix. Strategies to break the thermal blocking include high-loading filling [17], multi-filler coordination [18], interface processing [19, 20], alignment engineering [11, 12], and framework engineering [13]. The purpose of these strategies is to form high-efficiency and interconnected heat dissipation channels inside the composites, which is known as thermal percolation phenomena. The minimum concentration of thermal percolation phenomena is known as the percolation threshold. However, with the increase of fillers content, thermal conductivity is improved while Young's modulus will also sharply increase according to Eshelby's theory [14]. High thermal conductivity and low Young's modulus of materials are naturally a pair of contradictions. Hence, the thermal-mechanical tradeoff remains a challenge for TIMs. Fortunately, the thermal percolation threshold can be reduced by alignment engineering and framework engineering of fillers, especially for those anisotropic, rod-like and sheet-like fillers. As a result, a growing number of studies have focused on controlling the orientation of fillers and constructing three-dimensional (3D) thermally conductive frameworks by a variety of methods, including electric fields (electrostatic flocking [15, 16], electrospinning [21, 22]), magnetic field [23, 24], tape-casting, hot-pressing [25], vacuum filtration method [26–28], template method (ice-template [29–31], sugar-template [2], bubble-template [32]), etc. In general, microstructural regulations of fillers are realized by electric force, magnetic force and shear force in these methods. The mechanism of electric and magnetic force is similar, which is to control the fillers to align along the electric and magnetic field lines by the attraction and repulsion. Erb *et al* [33] investigated the rotation and orientation mechanism of fillers under external magnetic fields through experiments and theoretical energy models. In general, the electric and magnetic fields are usually used to control one-dimensional orientation, because the electric and magnetic field lines are always unidirectional and parallel. The alignment mechanism of shear force is still not clearly explained.

However, with the development of next-generation 5G devices and electric vehicles, complicated 3D-stacked integration is designed to realize more advanced functions within smaller size. Some tougher challenges have emerged, especially under complicated 3D distribution of heat sources, higher spatial power density and stricter local hotspots [34]. To tackle the increasingly severe heat dissipation issues in 3D-stacked electronics, we proposed a novel strategy combining vacuum filtration method and fluid control method to prepare the composites with the radial structure of CFs [27]. Theoretically, the arrangement of arbitrary two-dimensional shapes can be realized for heat sources with special shapes. In fact, the 2D design of orientation achieves a high-efficiency heat transport from heat regions, which significantly reduces the thermal resistance of diffusion. However, 3D-stacked integration brings complicated 3D distribution of heat sources, putting forward stricter requirements for heat dissipation channels. Therefore, the arbitrary shape 3D oriented regulation is critical to provide embedded and direct 3D heat pathways from heat sources to heat sink. Recent studies have explored the construction of 3D heat skeleton in composites. For example, Li *et al* [35] proposed a cost-effective foaming route to construct the 3D interconnected boron nitride (BN) network. However, the distribution and structure of 3D skeleton is hard to control, hence losing part of design freedom. Fortunately, 3D printing is an effective manufacturing method with high design freedom, offering unparalleled flexibility in achieving controlled composition, geometric shape, function, and complexity over traditional manufacturing methods. It is interesting that Kokkinis *et al* [36] opened the way towards the manufacturing of functional heterogeneous materials with exquisite microstructural features by magnetically assisted 3D printing method. Compton and Lewis [37] reported a new epoxy-based ink that enables 3D printing of cellular composites with controlled alignment of multi-scale, high aspect ratio fiber reinforcement to create hierarchical structures. The silicon carbide whiskers and carbon fibers (CFs) were added to the base formulation to create fiber-filled epoxy inks. However, these two methods are complicated and expensive because the

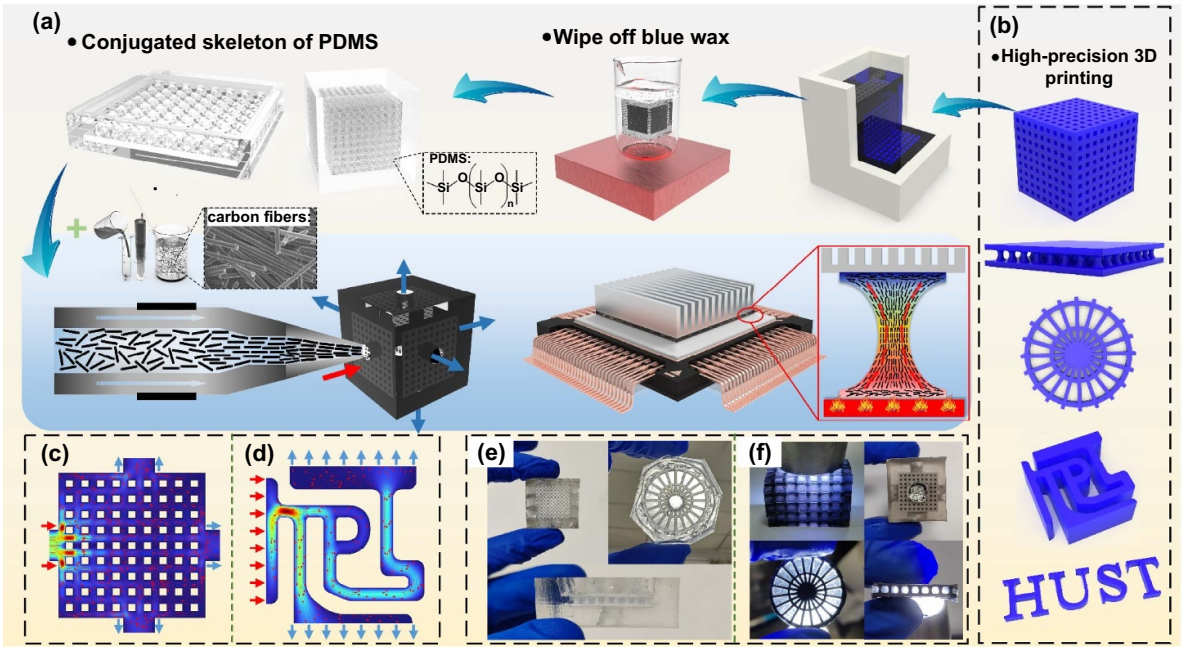

Figure 1. Overview of the 3D-PSO method. (a) Schematic diagram of 3D-PSO method. (b) 3D models prepared by high-precision 3D printing with blue wax. Fluid fields and streamlines in (c) 3D mesh-shape skeleton and (d) TPL-shape skeleton when mixture is injected. Optical images of (e) 3D conjugated skeletons and (f) composites.

experimental facility needs to be refitted to accomplish special functions. Hence, preparing composites with 3D heat dissipation channels of programmable shape still looks forward to a simper and cost-effective strategy.

Here, we proposed a 3D printing-assisted streamline orientation (3D-PSO) method to prepare CFMs with 3D programmable heat dissipation channels and excellent orientation of fillers inside. Figure 1 schematically shows the process of the 3D-PSO method. Different from existing 3D printing method [36, 37], we separated the preparation of arbitrary 3D framework from the process of alignment inside. The 3D-PSO method combines the shape-design capability of 3D printing and oriented control ability of fluid. In detail, 3D frameworks were fabricated by high-precision 3D printing with blue wax. Then, the blue wax frameworks were eliminated with corresponding fluid channels remaining in matrix, forming 3D conjugated skeletons. Fluid channels were sealed inside the matrix with an inlet and outlets. Finally, the mixture of fillers and matrix was injected into the fluid channels forming liquid streams inside, which drives fillers to orient along the streamlines. In addition, to demonstrate the mechanism of orientation, we carried out the mechanical analysis of fillers including the shear forces and normal pressure forces. Specifically, a variety of 3D models (including 3D mesh-shape skeleton, sandglass-shape skeleton, hub-shape skeleton, HUST-shape skeleton, and TPL-shape skeleton) were designed and fabricated. CFs composites and liquid metal (LM) composites were prepared with these models. 3D mesh-shape PDMS/LM composite showed a high thermal conductivity of 2.03 $W{\cdot}m^{-1}{\cdot}K^{-1}$) under filler loading of 34.8 vol% at 25 °C, reaching 79.3% of random PDMS/LM composites under filler loading of 69.8 vol%. 3D mesh-shape polydimethylsiloxane/CFs (PDMS/CFs) composites exhibit well local orientation, better thermal property and mechanical property in comparison to random PDMS/CFs composites with the same filler loading. The thermal conductivity enhancement efficiency (TCEE) of 3D mesh-shape PDMS/CFs composite is improved from 57.87% to 101.05% under filler loading of 5.2 vol% at 25 °C. Hence, the 3D-PSO method provides an effective way to improve both thermal and mechanical properties with lower filler loading. Benefiting from these 3D orientation microstructures, hub-shape PDMS/CFs composites and sandglass-shape PDMS/CFs composites demonstrated a better heat diffusion effect and heat dissipation effect than random composites, respectively. In the simulation of heat dissipation for 3D-stacked chips, the highest temperature with 3D-PSO composite is 42.14 °C lower than that with random composites. Furthermore, the TPL-shape PDMS/CFs composite exhibits an interesting 'TPL' shape, which is significative for the fine microstructure design and microfluidic study.

2. Mechanical analysis of fillers in matrix

As shown in figure 2(a), local orientation of fillers is observed in the random composite, even though the composite is irregular on the whole. The reason for this phenomenon is the multiple random flows in composites during preparation, resulting in consistent orientation inside flows and different orientations between flows. To demonstrate how the flow drives the orientation of fillers, force analysis of fillers in matrix during flowing was carried out. Taking CFs as fillers and PDMS as matrix, figure 2(b) shows representative CFs of different angles in the flow process of PDMS. In detail, there are two different

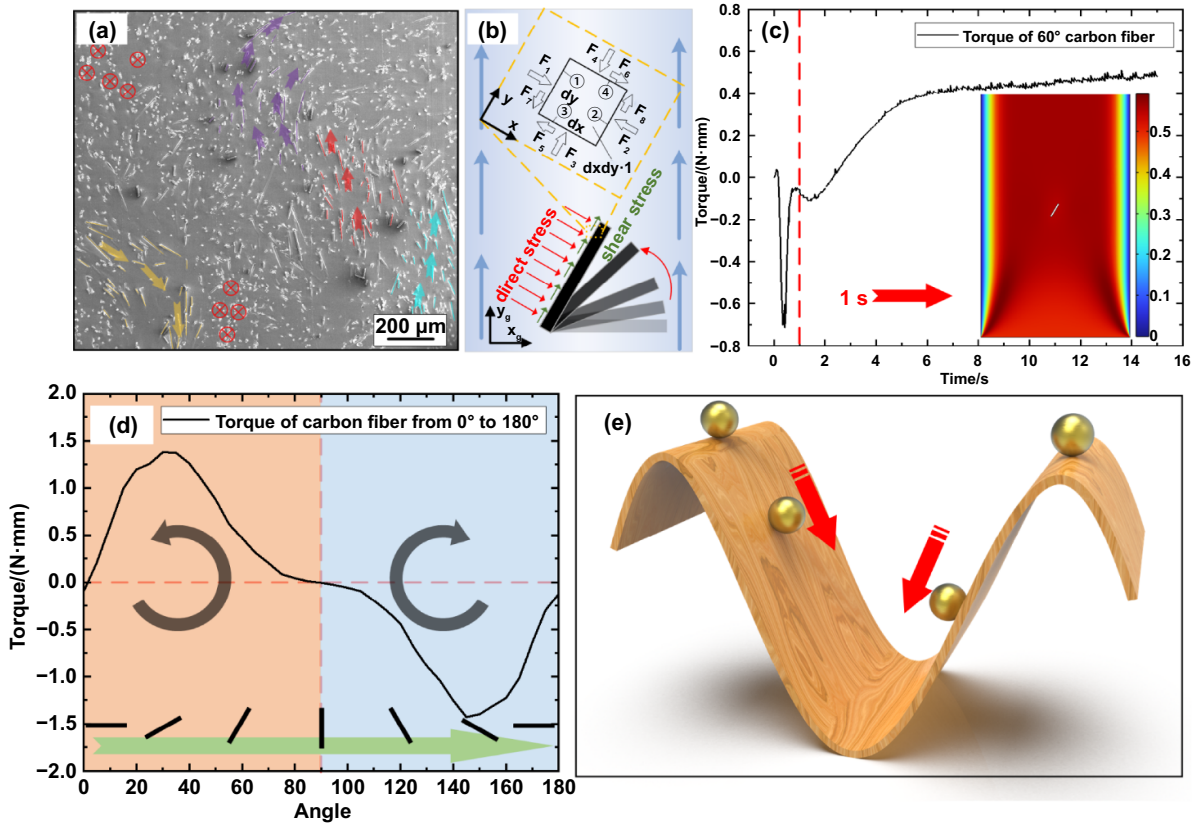

Figure 2. Microscopic characterization and mechanical analysis of the fillers in polymer matrix. (a) SEM image of random composite. (b) Force diagram of CFs in flowing matrix. (c) The torque curve of 60° CFs during the whole flow. (d) The final torques of CFs in different angles. (e) Movement of a ball over the peaks and valleys.

coordinate systems, where $x_g y_g$ coordinate system ($x_g y_g$-CS) is the global coordination system and xy coordinate system (xy-CS) is CFs-based coordinate system. A representative volume element of xy-CS is shown in figure 2(b). The forces acting on a surface are vectors, whose corresponding stress is regarded as a second order stress tensor. For 2D models, the stress tensor can be expressed as follows:

$$\tau_{ij} = \begin{bmatrix} \tau_{11} & \tau_{12} \\ \tau_{21} & \tau_{22} \end{bmatrix} = \begin{bmatrix} \sigma_x & \tau_{xy} \\ \tau_{yx} & \sigma_y \end{bmatrix} \tag{1}$$

Hence, the direct stress and shear stress (F_1–F_8) acting on the surface ①②③④ of the volume element can be expressed as follows:

$$\text{normal stress} \begin{cases} F_1 = \sigma_x \mathrm{d}y \bullet 1 \\ F_2 = \left(\sigma_x + \frac{\partial \sigma_x}{\partial x}\mathrm{d}x\right)\mathrm{d}y \bullet 1 \\ F_3 = \sigma_y \mathrm{d}x \bullet 1 \\ F_4 = \left(\sigma_y + \frac{\partial \sigma_y}{\partial y}\mathrm{d}y\right)\mathrm{d}x \bullet 1 \end{cases},$$

$$\text{shear stress} \begin{cases} F_5 = \tau_{yx} \mathrm{d}x \bullet 1 \\ F_6 = \left(\tau_{yx} + \frac{\partial \tau_{yx}}{\partial y}\mathrm{d}y\right)\mathrm{d}x \bullet 1 \\ F_7 = \tau_{xy} \mathrm{d}y \bullet 1 \\ F_8 = \left(\tau_{xy} + \frac{\partial \tau_{xy}}{\partial x}\mathrm{d}x\right)\mathrm{d}y \bullet 1 \end{cases}. \tag{2}$$

When the surface ② is the boundary of CFs, for CFs, the net surface force of ② in x direction and y direction can be expressed as follows, respectively:

$$\begin{aligned} F_x &= -F_2 = -\left(\sigma_x + \frac{\partial \sigma_x}{\partial x}\mathrm{d}x\right)\mathrm{d}y \bullet 1, \\ F_y &= -F_8 = -\left(\tau_{xy} + \frac{\partial \tau_{xy}}{\partial x}\mathrm{d}x\right)\mathrm{d}y \bullet 1. \end{aligned} \tag{3}$$

According to Stokes' Viscosity law, the relationship of velocity deformation rate and stress can be expressed as follows:

$$\begin{aligned} &\tau_{xy} = \tau_{yx} = \mu\left(\frac{\partial u}{\partial y} + \frac{\partial v}{\partial x}\right),\ \sigma_x = -p + 2\mu\frac{\partial u}{\partial x}, \\ &\sigma_y = -p + 2\mu\frac{\partial v}{\partial y}. \end{aligned} \tag{4}$$

Taking equation (4) into equation (3), the net surface force in x direction and y direction can be converted as follows:

$$\begin{aligned} F_x &= -\left(-p + 2\mu\frac{\partial u}{\partial x} + \frac{\partial\left(-p + 2\mu\frac{\partial u}{\partial x}\right)}{\partial x}\mathrm{d}x\right)\mathrm{d}y \bullet 1 \\ F_y &= -\left(\mu\left(\frac{\partial u}{\partial y} + \frac{\partial v}{\partial x}\right) + \frac{\partial\left(\mu\left(\frac{\partial u}{\partial y} + \frac{\partial v}{\partial x}\right)\right)}{\partial x}\mathrm{d}x\right)\mathrm{d}y \bullet 1 \end{aligned}. \tag{5}$$

Hence, when the flow fields are calculated, the torque of the fluid acting on the fillers can be calculated as follows:

$$T_{\text{filler}} = \oint_{\substack{\text{boundary}\\ \text{of filler}}} (y_0 - y) F_x + \oint_{\substack{\text{boundary}\\ \text{of filler}}} (x_0 - x) F_y \tag{6}$$

where (x_0, y_0) are the coordinates of CFs barycenter. It can be seen that T_{filler} can be calculated out once the velocity field and pressure field are solved. However, it is fairly complicated to solve the time-varying flow field because the angle of CFs will change with the flow. Hence, we propose to fix the angle of CFs unchanged, and then calculate the torque curve over time. The flow fields in $x_g y_g$-CS are simulated by finite element simulation, and then are converted to flow field in xy-CS for calculating torque according to the angle of CFs. The same operations are carried out for every angle of CFs. In detail, to obtain the torque of CFs at different angles, the flow fields were simulated with CFs' angle ranging from 0° to 180°. The CFs' angle is defined as the angle between the long axis of CFs and the x-axis. CFs is placed in flowing PDMS and flow with the matrix, where the angle of CFs is fixed but position not. In addition, the flow process was simulated for 15 s to ensure the torque reaching the final stable state. According to equation (6), CFs torques were obtained. Figure 2(c) shows the torque curve of 60° CFs during the whole flow and the flow field image at 1 s. It can be observed that the torque reaches stable state after 7 s. To eliminate error, the average torque from (10 to 15) s was calculated and regarded as the final torque in corresponding angle. Figure 2(d) shows the final torques with the angle vary from 0° to 180°, which are calculated by the same operations. When CFs are oriented between 0° and 90°, the torques are greater than zero, indicating that anticlockwise torques would drive the CFs to rotate towards 90°. When CFs are oriented between 90° and 180°, the torques are lower than zero, indicating clockwise torques which would also drive the CFs to rotate towards 90°. Hence, the CFs would orient towards 90° no matter what the angle is, which means that CFs would orient along streamline. It is interesting that 0° or 180° can be regarded as balanced systems, which is the same as 90° on account of the symmetric structure. However, once there is any disturbance, the balance of 0° or 180° would be destroyed and drove new balance at 90°. The balance of 0° or 180° can be regarded as a metastable state. The situation is quite similar to the movement of a ball over the peaks and valleys, as shown in figure 2(e). The peaks and valleys can all meet the condition of balance. However, once there is any disturbance in the peaks, the ball would move towards the valley and build a new balance. As a result, the model exhibits the force analysis and reveals the mechanism of filler orientation along streamlines, which is the combined result of normal pressure and shear force. The supported videos show how CFs orient with the fluidic flow.

3. Results and discussion

3.1. Fabrication of composites

CFs are typical one-dimensional material with high axial thermal conductivity (TC, 600 $\text{W}\cdot\text{m}^{-1}\cdot\text{k}^{-1}$), which is selected as the thermal conductive fillers in this work. According to the force analysis before, the flow can effectively drive CFs orient along streamlines. In addition, 3D printing exhibits an excellent shape-design capability. Hence, the 3D-PSO method was proposed to construct the CFMs with 3D programmable heat dissipation channels and excellent orientation of fillers inside. Figure 1(a) shows the process of the 3D-PSO method, which combines the shape-design capability of 3D printing and control ability of fluid. First, complicated 3D models are fabricated by high-precision 3D printing with blue wax. Subsequently, matrix is poured into a mold to immerse the models and fill the gaps of models. Second, cured samples are immersed in ethyl alcohol on the heat plate of 150 °C to remove blue wax. After multiple cleaning, blue wax is removed with matrix remaining, which forms 3D conjugated skeletons of matrix. The original position of blue wax turns into fluid channels. Third, CFs and matrix are mixed and poured into syringe. At last, the syringe is connected to the 3D conjugated skeletons through a hole as fluid inlet with other holes as fluid outlets. The mixed fluid is injected into the 3D conjugated skeletons and drives CFs to orient along streamlines. Figures 1(b) and (c) show interesting fluid fields and streamlines inside the 3D conjugated skeletons, which are realized by designing fluid channels. Hence, CFs would orient along the fluid channels and form heat dissipation channels inside during the process of injection. As a result, complicated 3D structures of fillers can be realized by the design of fluid channels.

To realize different functions, complicated microstructures were designed and fabricated, as shown in figure 3(a). Specifically, 3D mesh-shape composite was fabricated with crisscrossed 3D heat dissipation channels. Sandglass-shape composite was fabricated to improve its through-plane thermal conductivity. Hub-shape composite was fabricated to enhance in-plane heat diffusion. TPL-shape composite and HUST-shape composite were fabricated to show the control ability of liquid for CFs. In addition, PDMS/CFs and PDMS/LM composites with different microstructures were prepared. Figures 3(b), (c), (e) and (f) show the different sections of the 3D mesh-shape PDMS/CFs composites. It can be observed that CFs orient differently in different fluid channels, as shown by the red arrows, which is similar to the streamlines of simulation in figure 1(b). It is worth noting that the cross symbol represents that CFs orient along vertical direction of the section. Figure 3(d) shows the section of sandglass-shape composite. CFs orient horizontally or vertically to the section due to the in-plane diffusion of liquid, which provides rapid heat diffusion at the top and bottom of composites. Moreover, CFs orient vertically in the middle channels of the composites which

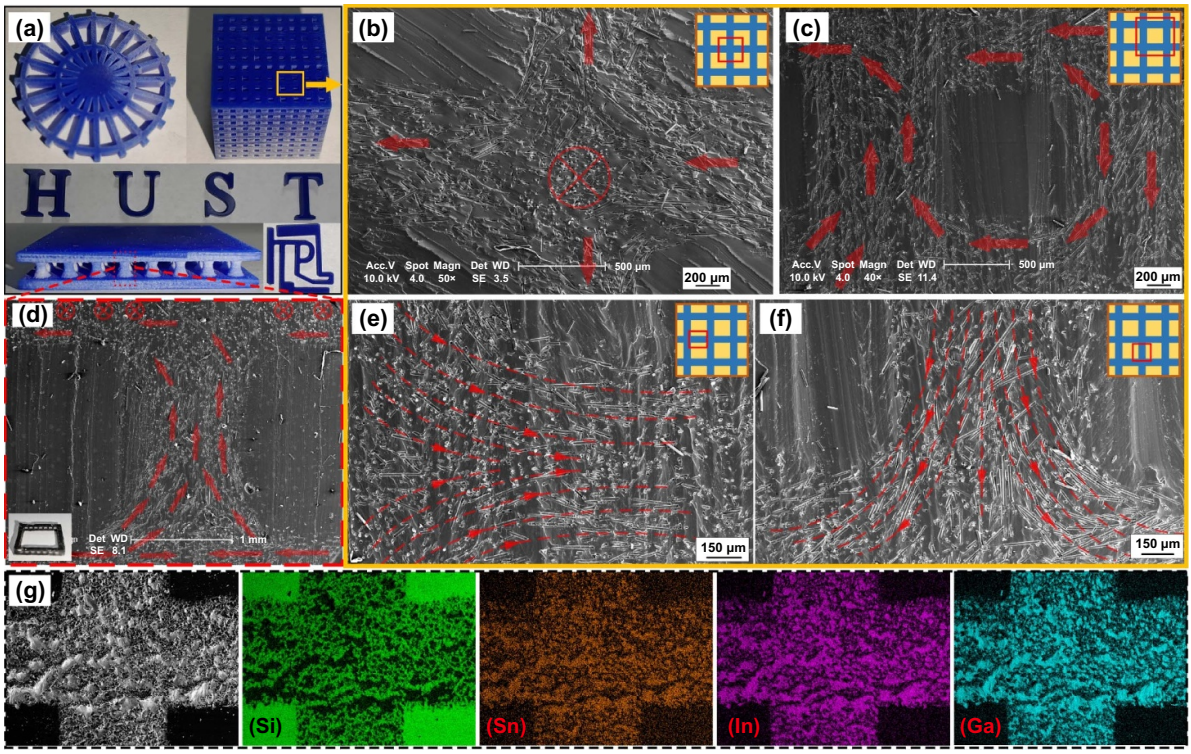

Figure 3. Microstructures fabricated by the 3D-PSO method. (a) Optical images of different models. (b), (c), (e) and (f) SEM images of 3D mesh-shape PDMS/CFs composites in different position. (d) SEM image of sandglass-shape PDMS/CFs composite. (g) Energy spectrum of 3D mesh-shape PDMS/LM composite.

provides rapid heat conduction between the top and bottom. Hence, the through-plane thermal conductivity of sandglass-shape composite is enhanced. In addition, 3D mesh-shape PDMS/LM composite was prepared by injecting a mixture of $Ga_{67}In_{20.5}Sn_{12.5}$ (69.8 vol%) and PDMS (30.2 vol%) into 3D mesh-shape fluid channels to make full use of the thermal performance of 3D thermal frameworks. Figure 3(g) shows the energy spectrum of different elements, where element Si originates from PDMS, and elements Sn, In, and Ga originate from LM, respectively. The sharp boundary shows the excellent ability of 3D-PSO method for manufacturing complicated microstructures.

In addition, to exhibit the excellent control ability of fluid, composites were fabricated with TPL-shape skeleton. Figures 4(a)–(c) show local images of TPL-shape PDMS/CFs composites, where conjugated skeleton was fabricated by pure PDMS. The clear orientation of CFs can be observed inside fluid channels of letters. Most CFs were driven to orient along streamlines by fluid with a small number of disorder due to the whirlpools. Particularly, figure 4(b) shows excellent orientation of the Letter 'P'. Furthermore, when conjugated skeleton was fabricated with random PDMS/CFs composite, TPL-shape-random PDMS/CFs composites with locally special orientation were fabricated. Figure 4(d) shows the optical image of TPL-shape-random PDMS/CFs composites. Figures 4(e)–(h) show SEM images of corresponding position in figure 4(d). The red arrows show the local direction of CFs, which is consistent with letter fluid channels. Figures 4(f)–(g) show the orientation of 'T' 'P' and 'L' shapes, respectively. It is interesting that the orientation of other positions is chaotic and disordered, showing clear boundary with letter fluid channels. In addition, HUST-shape PDMS/CFs composites are shown in figure S3. As a result, 3D PSO method exhibits excellent control ability of fillers by controlling the fluid dynamics. Combined with the shape design ability, the 3D PSO method can construct programmable heat dissipation channels with a targeted orientation of fillers inside.

3.2. *Characterization of thermal and mechanical properties*

Thermal conductivity of a composite material is mainly determined by the intrinsic thermal conductivity of its matrix/-fillers, the mass fraction of fillers, and the microscopic orientation and distribution of fillers. High filler loading contributes to higher thermal conductivity while causing severe sacrifice in mechanical flexibility, which is unsuitable for the application of TIMs. The 3D PSO method provides a novel way to achieve both high thermal and mechanical properties. To analyze the thermal and mechanical performances of different composites, a series of material characterizations, including differential scanning calorimetry (DSC), laser flash analysis (LFA), thermal mechanical analysis (TMA), dynamic mechanical analysis (DMA), and tensile test were conducted. In detail, the thermal diffusion coefficients (TD) of composites, including 3D mesh-shape PDMS/CFs composite, sandglass-shape PDMS/CFs composite, random PDMS/CFs composites and random PDMS/LM composite were measured, as shown in figure 5(a). The random PDMS/CFs composites of

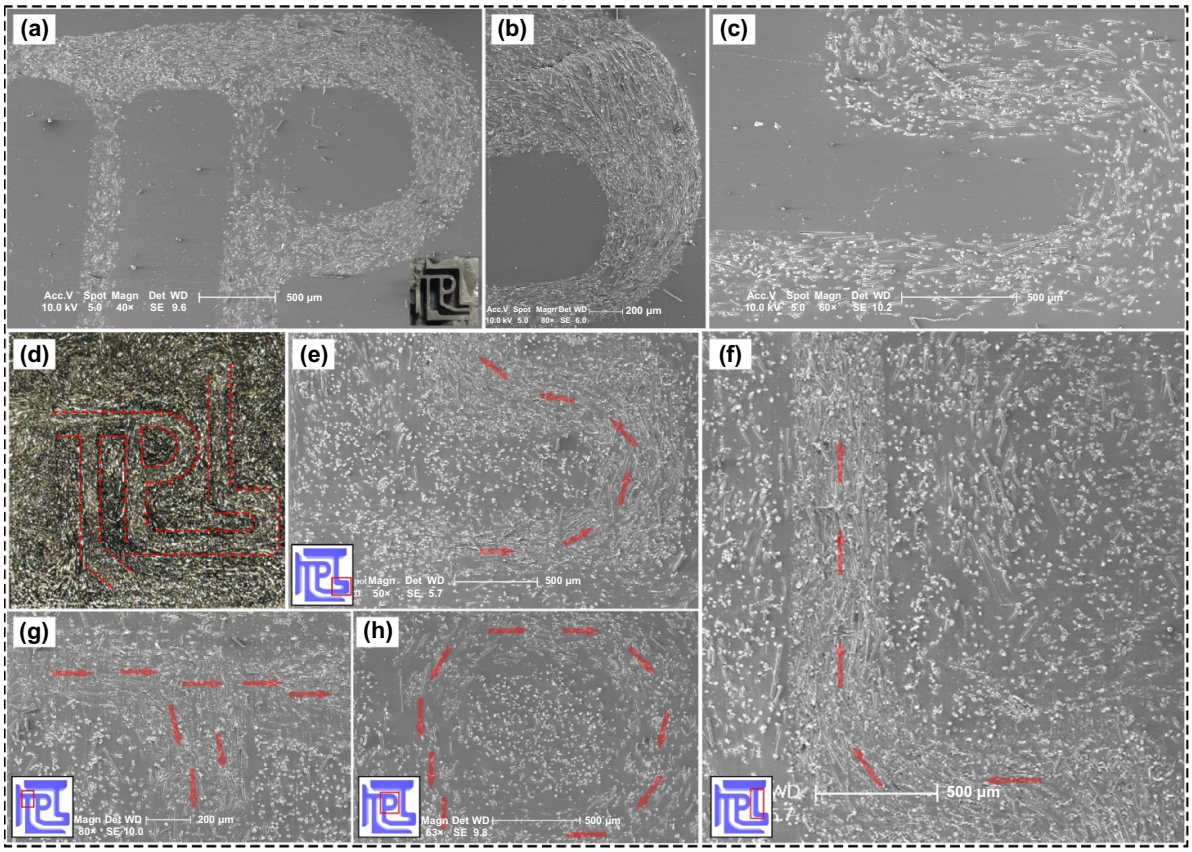

Figure 4. Microstructures in the TPL-shape composites. (a)–(c) SEM images of TPL-shape PDMS/CFs composites. (d) Optical image of TPL-shape-random PDMS/CFs composites. (e) SEM images of 'P–L' transitional channel. SEM images (f) 'T', (g) 'P', and (h) 'L' in TPL-shape-random PDMS/CFs composites.

10 wt% (4.9 vol%) and 20 wt% (10.4 vol%) were prepared by directly mixing the PDMS and CFs. For the 3D mesh-shape PDMS/CFs composite, a PDMS/CFs mixture containing 20 wt% of CFs was injected into the fluid channels (in which the 3D conjugated skeleton was made of pure PDMS). According to the volume fraction of fluid channels (50 vol%), the average mass fraction of 3D mesh-shape PDMS/CFs composite was calculated as 10.6 wt% (5.2 vol%). Similarly, the average mass fraction of sandglass-shape PDMS/CFs composite was calculated as 12.0 wt% (5.9 vol%). Random PDMS/LM composites of 34.8 vol% and 69.8 wt% were prepared. The average volume fraction of 3D mesh-shape PDMS/LM composite was calculated as 34.8 vol%. With the results of density and specific heat capacity, the thermal conductivities (TC) of these composites were calculated, as shown in figure 5(b). It is worth noting that 3D mesh-shape PDMS/CFs composite (0.94 $W{\cdot}m^{-1}{\cdot}k^{-1}$, 5.2 vol%) showed a higher TC than random PDMS/CFs composite-1 (0.58 $W{\cdot}m^{-1}{\cdot}k^{-1}$, 4.9 vol%) and similar TC to random PDMS/CFs composite-2 (0.96 $W{\cdot}m^{-1}{\cdot}k^{-1}$, 10.4 vol%) at 25 °C. The improvement implies the formation of heat dissipation pathways because of the orientation of CFs inside the fluid channels. Sandglass-shape PDMS/CFs composite showed slightly lower TC than that of 3D mesh-shape PDMS/CFs composite on account of its in-plane orientation on the top and bottom. It is noted that the TC of 3D mesh-shape PDMS/LM composite (2.03 $W{\cdot}m^{-1}{\cdot}k^{-1}$, 34.8 vol%) is 5.8 times of random PDMS/LM composite-1 (0.35 $W{\cdot}m^{-1}{\cdot}k^{-1}$, 34.8 vol%) and 79.3% of random PDMS/LM composite-2 (2.56 $W{\cdot}m^{-1}{\cdot}k^{-1}$, 69.8 vol%). The improvement is attributed to the heat dissipation channels formed after the blue wax skeleton is dissolved.

As a result, 3D-PSO method provides a practical way to realize considerable improvement of TC with a half of filler loading by ingenious design of 3D models. The TCEE of composite describes the efficiency of filler of per unit volume in contributing to the thermal enhancement, which is defined as equation (7):

$$\mathrm{TCEE} = \frac{k - k_\mathrm{m}}{100 V_\mathrm{f} k_\mathrm{m}} \tag{7}$$

where k and k_m are the TC of the composite and pure matrix, respectively. V_f represents the volume fraction of filler in the composite. As shown in figure 5(c), the TCEE of 3D mesh-shape PDMS/CFs composite was 101.05% under filler loading of 5.2 vol% at 25 °C. The TCEE of random PDMS/CFs composite-1 was 57.87% under filler loading of 4.9 vol% at 25 °C. In a similar volume fraction, the TCEE of 3D mesh-shape PDMS/CFs composite was improved, which is mainly attributed to the local aggregation of fillers in fluid channels and oriented structure of filler. These characteristics improve

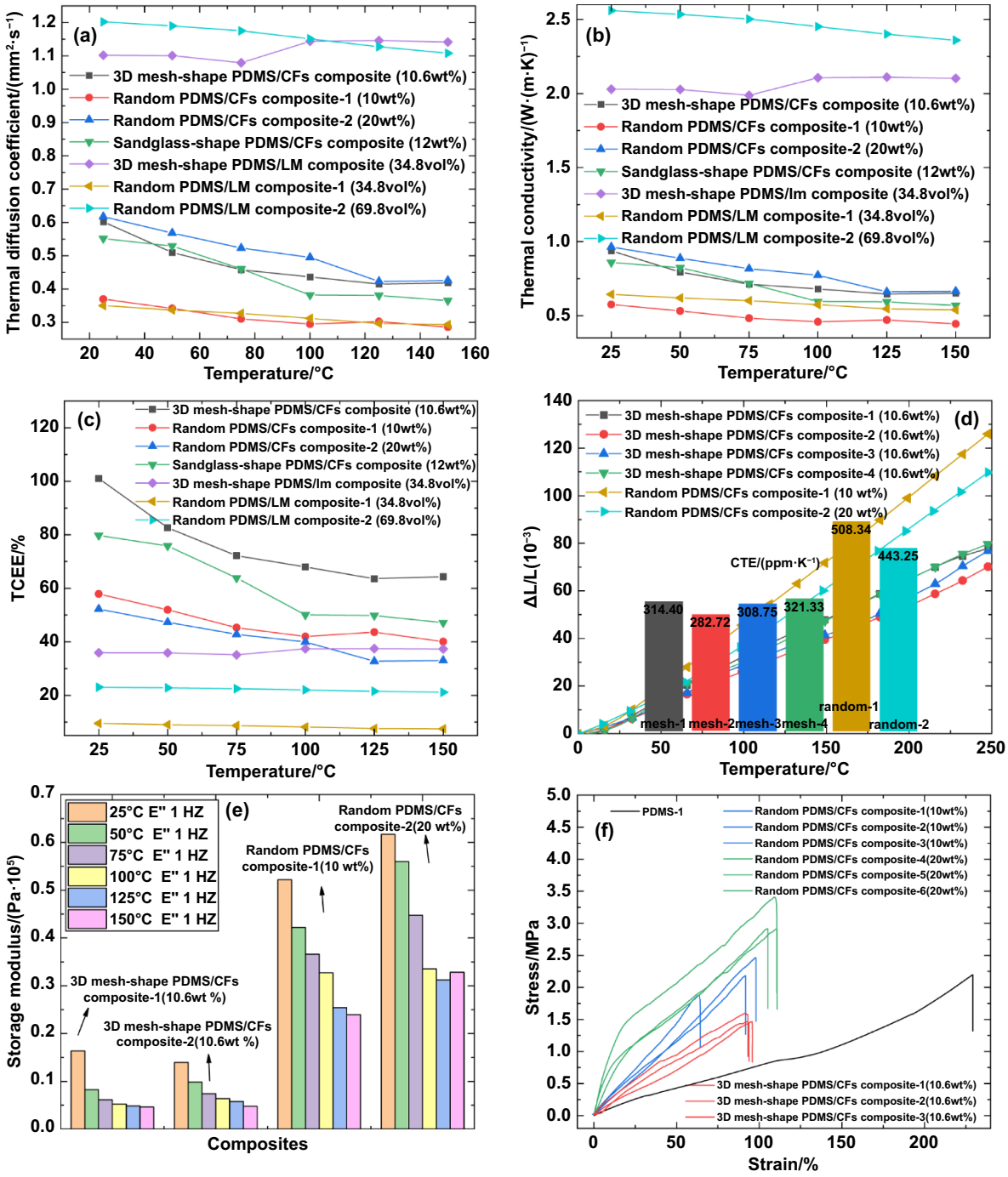

Figure 5. Thermal and mechanical properties of different composites. (a) TD, (b) TC and (c) TCEE of different composites. (d) Length expansion curves of different composites between 0 °C and 250 °C. (e) The storage modulus of different composites under 1 Hz. (f) The stress-strain curves of different composites.

the probability of fillers to connect with each other under the same mass fraction, which is crucial for forming thermal percolation pathways. The 3D mesh-shape PDMS/LM composite showed a higher TCEE than random PDMS/LM composite only on account of local aggregation of fillers in fluid channels. Figure 5(d) illustrates the coefficient of thermal expansion (CTE) of some composites between 0 °C and 250 °C, which reflects their thermal stability. 3D mesh-shape PDMS/CFs composites showed a lower CTE even though compared with random composites with higher mass fraction, which provides higher thermal stability during operation. This is attributed to the ordered orientation of fillers and negative CTE of CFs in axial direction [38, 39].

Moreover, the mechanical properties of those composites were measured and analyzed by DMA test and tensile test. Figure 5(e) illustrates the DMA measurement result under 1 Hz. Interestingly, 3D mesh-shape PDMS/CFs composites showed lower storage modulus than that of random

Table 1. Thermal and mechanical properties of different composites.

Sample	Mass fraction /(%)	Volume fraction/%	TC in 25 °C/ ($W \cdot m^{-1} \cdot K^{-1}$)	TCEE in 25 °C/%/	Elasticity modulus (MPa)
3D mesh-shape PDMS/CFs composite	10.6	5.2	0.94	101.05	1.57
Sandglass-shape PDMS/CFs composite	12	5.9	0.86	79.77	—
Random PDMS/CFs composite-1	10	4.9	0.58	57.87	2.55
Random PDMS/CFs composite-2	20	10.4	0.96	52.22	6.39
3D mesh-shape PDMS/LM composite	77.18	34.8	2.03	35.90	—
Random PDMS/LM composite-1	77.08	34.8	0.35	9.48	—
Random PDMS/LM composite-2	93.58	69.8	2.56	23.02	—

PDMS/CFs composites. The result of tensile test indicated the same conclusion, as shown in figure 5(f). Elasticity modulus of random PDMS/CFs composite in 10 wt% and 20 wt% were 2.55 MPa and 6.385 MPa, respectively. 3D mesh-shape PDMS/CFs composites showed lowest elasticity modulus of 1.57 MPa, which is mainly attributed to their concentrated filler networks that cause less influence on the flexibility of PDMS matrix. Table 1 shows thermal and mechanical properties of different composites in values for intuitively comparing the advantages of 3D-PSO method.

3.3. Application and comparison of composites

The 3D-PSO method provides a programmable design ability for the construction of heat dissipation channels. Different structures are designed and prepared to realize different applications. Figures 6(a) and (b) show different orientations and distributions of random PDMS/CFs composite and 3D mesh-shape PDMS/CFs composite, respectively. The local areas are cut out and shown in figures 6(c) and (d) at 10.5 vol%. Experiment I were designed to show the actual effect of heat dissipation channels. In detail, random PDMS/CFs composite-1, random PDMS/CFs composite-2, and 3D mesh-shape PDMS/CFs composite were placed on a heating plate with a constant temperature of 120 °C, simultaneously. Figure 6(e) shows the specific experimental setup and infrared images of experiment I, with optical photograph of samples. Random PDMS/CFs composite-1 showed the lowest temperature due to its lowest thermal conductivity. 3D mesh-shape PDMS/CFs composites show a similar temperature field with random PDMS/CFs composite-2, indicating similar thermal conductivity and good heat conduction due to the established heat dissipation channels. These results are consistent with the measured results of thermal conductivity. In 3D mesh-shape PDMS/CFs composites, CFs are more inclined to be connected and oriented along fluid channels. Hence, the thermal flow will be guided by ordered and connected fillers along fluid channels as shown in figure 6(d).

For hub-shape PDMS/CFs composite, heat dissipation channels are designed to realize faster heat diffusion from the central heat source. Experiment II was designed to verify the actual TD effect as shown in figure 6(f). In detail, Φ5 mm ceramic heating sheets (1.5 V, 2 W) were placed under the center of samples to simulate micro heat source. Customized polyphenylene sulfide boards were placed to fix samples and heat sources with bolts and nuts. A torque of 0.13 N·m was supplied on the bolts and nuts to ensure different samples sustain the same pressure. All ceramic heating sheets were organized in series to ensure the same electric current. Thermocouples were placed upon ceramic heating sheets to record its temperature. Figure 6(h) shows infrared images of top surface at different time. Hub-shape PDMS/CFs composite showed higher temperature on the edge due to vertical heat dissipation channels of central and radial heat dissipation channels in plane. It is worth noting that ceramic heating sheets with hub-shape PDMS/CFs composite showed the lowest temperature even at the lowest mass fraction. This is mainly because that heat was quickly conducted, diffused and then dissipated to environment. These results prove that hub-shape PDMS/CFs composite has a superior ability to conduct and expand heat from micro heat sources at a lower mass fraction.

Sandglass-shape PDMS/CFs composite was designed to realize quick heat conduction as TIMs. To verify its effect in heat dissipation system, experiment III was designed and conducted. Figure 7(a) shows the experimental set-up. Square ceramic heating sheets (20 mm × 20 mm) are used to simulate computer's CPU as heat sources. Samples were placed between heat sources and heat sink as TIMs. Thermocouples were placed upon ceramic heating sheets to record its temperature. A torque of 0.13 N·m was supplied on the bolts and nuts to ensure different samples sustain the same pressure. Ceramic heating sheets were connected in series to ensure the same

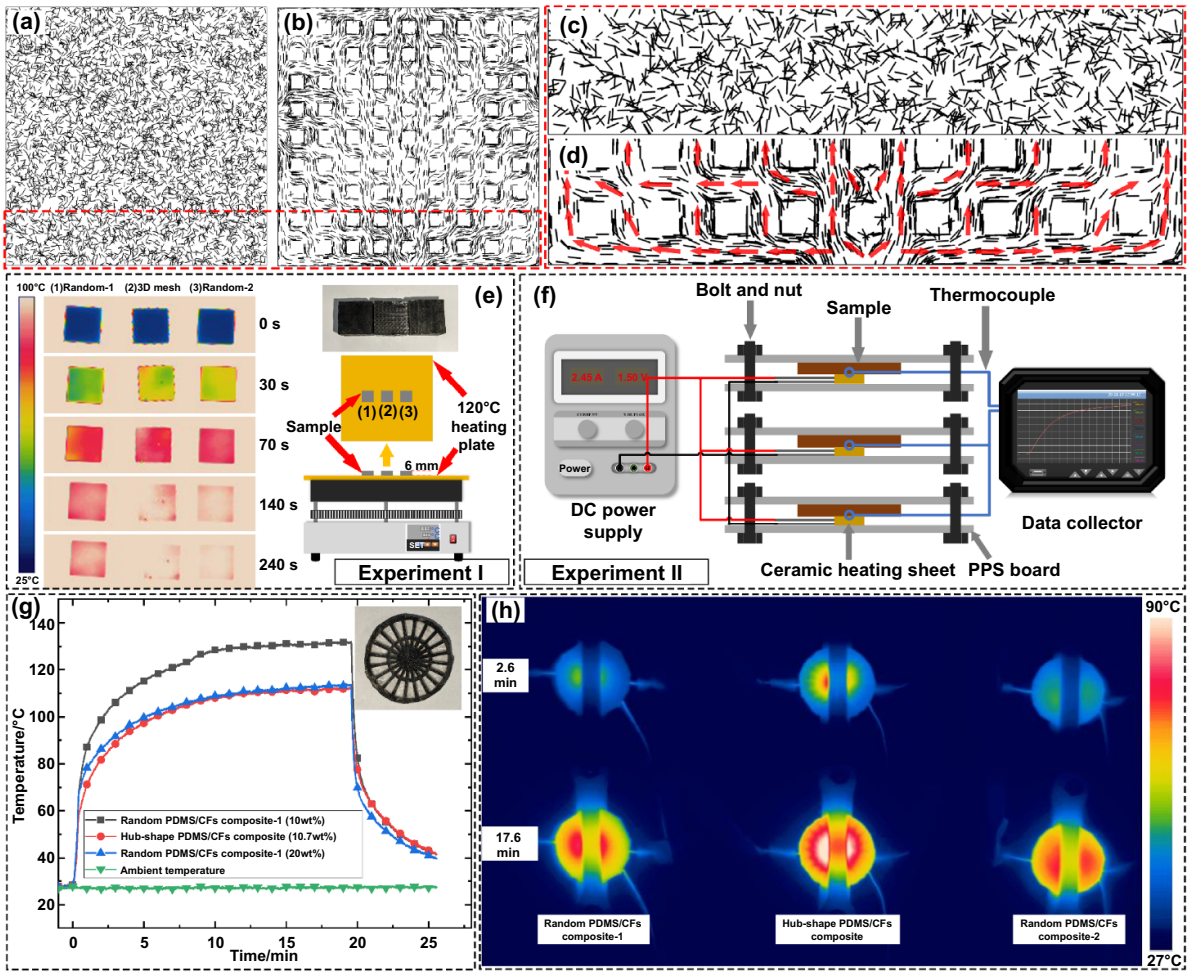

Figure 6. Heat transfer capability demonstration of the random and 3D mesh-shape PDMS/CFs composites. Orientation and distribution of fillers in (a) random PDMS/CFs composite and (b) 3D mesh-shape PDMS/CFs composite. Local enlarged views of (c) random PDMS/CFs composite and (d) 3D mesh-shape PDMS/CFs composite. (e) Setup and infrared thermograms of Experiment I for comparing through-plane heat transfer effect. (f) Setup of Experiment II for comparing in-plane heat transfer effect. (g) The core temperature curves of ceramic heating sheets in Experiment II over time. (h) Infrared thermograms of Experiment II.

electric current. Similarly, random PDMS/CFs composite-1 and random PDMS/CFs composite-2 were used for comparison. Figure 7(b) shows the temperature curve of ceramic heating sheets with different samples. The ceramic heating sheet with the sandglass-shape PDMS/CFs composite showed the lowest temperature in low filler loading because of the special orientation structure. As shown in images (1) and (2) of figure 7(b), sandglass-shape structure connects upper and lower surfaces, forming continuous thermal bridge. Fluid droves fillers to form programmable orientation structure along fluid channels, which significantly improved heat conduction efficiency.

Figure 7(c) shows the infrared image of experiment III. The lowest temperature of sandglass-shape PDMS/CFs composite showed its terrific application potential in the heat dissipation as TIMs with a lower filler loading. Furthermore, with the development of 3D-stacked chips, electronic devices are getting more compact. Figure 7(d) shows the simple 3D-stacked structure with local hotspots. It is impossible to fix fins on the upper and lower surfaces. With 3D-PSO method, we can design and prepare the targeted and oriented 3D heat dissipation channels according to the distribution of heat sources as shown in orange structure of figure 7(d). The heat was transported to the side surfaces, and then transported to heat sinks. Figure 7(e) shows the simulated results of heat dissipation. The left part and right parts are random PDMS/CFs composite and 3D-PSO PDMS/CFs composite with the same filler loading, respectively. The detailed setup is shown in Supporting Information. The highest temperature of 3D-stacked chips with the 3D-PSO composite was 42.14 °C lower than that with the random composite.

4. Conclusion

In summary, we reported a 3D-PSO method by combining 3D printing with orientation control of fluid. The 3D-PSO method features both the shape-design capability of 3D printing and filler control ability of fluid. The mechanism of streamline-guided filler orientation was revealed by force

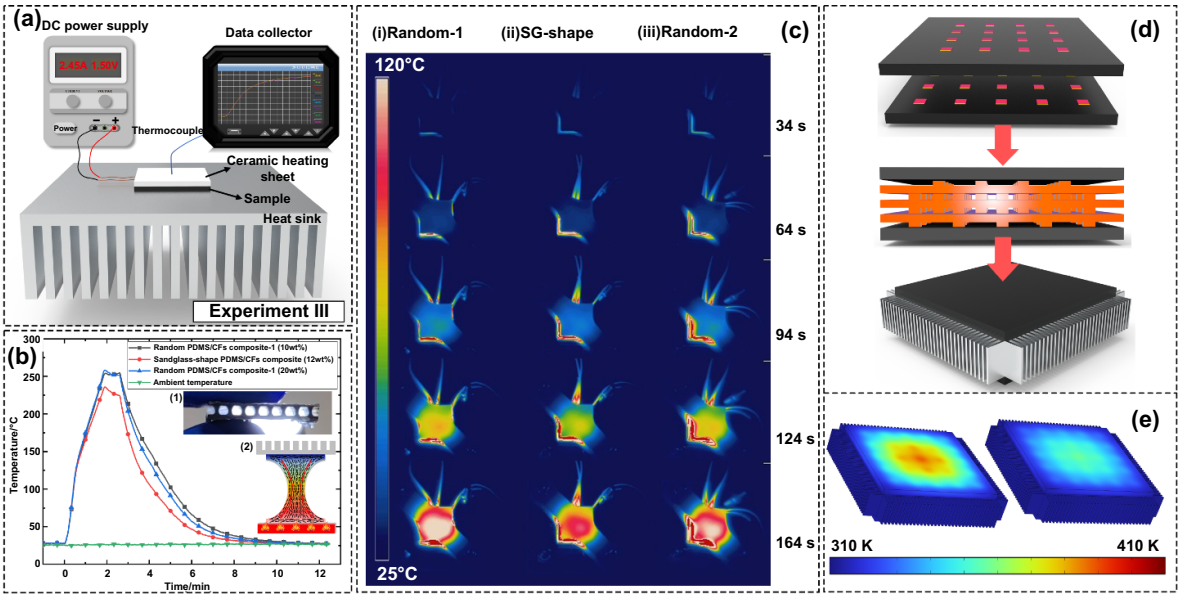

Figure 7. Interfacial heat transfer ability validation of different composites. (a) Setup of Experiment III for comparing actual heat dissipation effect as TIMs. (b) The core temperature curves of ceramic heating sheets in Experiment III over time. (c) Infrared thermograms of Experiment III. (d) Schematic showing the packaging structure of 3D-stacked chips. (e) Simulated temperature field of 3D-stacked chips with random PDMS/CFs composite (left) and 3D-PSO PDMS/CFs composite (right) as the TIMs.

analysis of fillers in matrix. Fillers tend to orient along streamlines under the combined action of shear force and normal pressure because of the minimum torque. Different composites were prepared with complicated heat dissipation channels to realize different functions. 3D mesh-shape, sandglass-shape and TPL-shape PDMS/CFs composite exhibited the programmable ability of 3D-PSO method to prepare complicated microstructures and good orientation. 3D mesh-shape PDMS/LM composite showed a high thermal conductivity of 2.03 $W{\cdot}m^{-1}{\cdot}k^{-1}$ under filler loading of 34.8 vol%, which is 5.8 times of random PDMS/LM composites under the same filler loading. The TCEE of 3D mesh-shape PDMS/CFs composite reached 101.05% under filler loading of 5.2 vol%. The thermal stability of 3D mesh-shape PDMS/CFs composite was enhanced even compared to high filler loading. These are attributed to local aggregation and orientation structure of fillers in fluid channels, which contribute to thermal percolation phenomena. In addition, the mechanical property of 3D mesh-shape PDMS/CFs composite was also improved because of the exist of pure matrix, exhibiting the lowest elasticity modulus of 1.57 MPa at 10.6 wt%. Moreover, hub-shape PDMS/CFs composite and sandglass-shape PDMS/CFs composite exhibited better TD ability and better heat dissipation effect as TIMs even in lower filler loading. In the simulation of heat dissipation for 3D-stacked chips, the highest temperature with the 3D-PSO composite is 42.14 °C lower than that with random composites. As a result, the 3D-PSO method demonstrates a programmable design ability for 3D microstructures and good orientation control ability, which presents the potential to build complicated heat dissipation channels inside composites and realize superior thermal and mechanical performances in lower filler loading. With programmable microstructure and orientation of fillers, the 3D-PSO method is promising to achieve efficient heat dissipation for complicated 3D-stacked chips integration.

5. Experiment section

5.1. Materials

CFs with a length of 200 μm (K223HM) and axial TC of 600 $W{\cdot}m^{-1}{\cdot}k^{-1}$ were purchased from Mitsubishi Chemical. PDMS was purchased from Dow Corning Co., Ltd and used as the polymer matrix. LM ($Ga_{67}In_{20.5}Sn_{12.5}$) is also selected as fillers. All chemicals were directly used without further purification. 3D skeletons of programmable shapes were prepared by high-precision 3D printing with blue wax.

5.2. Preparation of 3D conjugated skeletons

First, 3D skeletons of arbitrary shape were prepared by high-precision 3D printing with blue wax. Second, PDMS was prepared by mixing component A and component B by 10:1. Then alternating cycles of vacuum were applied in the mixed PDMS to remove bubbles. Then, the 3D skeletons were placed in curing vessel and PDMS is poured into the vessel, ensuring PDMS to fully cover the whole skeletons. Third, continuous degassing was carried out every 5 min. This process was carried out repeatedly for 5 times to ensure that PDMS was fully impregnated into the interspace of skeletons. Fourth, the vessel was placed at 25 °C for 24 h to ensure the complete curing of PDMS. Fifth, the cured PDMS was pierced to expose the blue wax inside. Sixth, the cured PDMS was added into the boiling alcohol to melt and scour off the blue wax. The process was carried out repeatedly for 5 times to ensure that blue wax is eliminated completely. At last, 3D conjugated skeletons

made up of pure PDMS were obtained. Specifically, 3D mesh-shape skeleton, sandglass-shape skeleton, hub-shape skeleton, HUST-shape skeleton and TPL-shape skeleton were designed and prepared.

5.3. Preparation of composites with programmable heat dissipation channels

When 3D conjugated skeletons are obtained by dissolving blue wax, the space formerly occupied by blue wax forms fluid channels. Then, matrix/fillers mixture is prepared in a certain proportion. The mixture is poured into injector and degassed for 20 min. Subsequently, the injector and 3D conjugated skeletons are connected and fixed by hot melt glue. The connected channel is set as inset. Some channels are made as outlets. After that, 3D conjugated skeletons are degassed by outlets. Then, mixture is slowly injected to fluid channels. All outlets are set as only outlets in turn by block off other outlets, to ensure full flow in fluid channels. When all fluid channels are full filled, the total setup is placed at 25 °C for 24 h to ensure the complete curing of mixture. In this work, CF and LM ($Ga_{67}In_{20.5}Sn_{12.5}$) are chosen as fillers. Specifically, 3D mesh-shape PDMS/CFs composites, 3D mesh-shape PDMS/LM composites, sandglass-shape PDMS/CFs composites, hub-shape PDMS/CFs composites, HUST-shape PDMS/CFs composites, and TPL-shape PDMS/CFs composites were prepared.

5.4. Characterization

The microscopic morphology was tested by a field-emission scanning electron microscope (FESEM, Sirion 200) to characterize the morphologies of composites. The optical images were obtained by stereo microscope (Stemi 508). Through-plane TC was calculated according to the equation $\kappa = \alpha \times \rho \times C$, where κ, α, ρ, and C correspond to TC, TD, density, and specific heat capacity, respectively. The through-plane TD of composites was measured by LFA 467 (Netzsch). The specific heat capacities of matrix and fillers were measured by DSC (Diamond DSC, PerkinElmer Instruments). The specific heat capacities and density of composites were calculated according to mass fraction. In addition, the CTE of the composites in through-plane direction was measured by static thermomechanical analysis (TMA, Q400EM) with a temperature range from 0 °C to 250 °C. The storage moduli of composites were measured by dynamic TMA (Diamond DMA) in compress mode in 1 HZ. The tensile tests of composites were measured with a loading rate of 1 mm·min^{-1} by Instron 6 800. The infrared thermograms were recorded by Infrared thermograph (FLIR SC620).

Acknowledgment

This work is supported by the National Natural Science Foundation of China (Grant No. 52106089), and the National Key R&D Project from Ministry of Science and Technology of China (Grant No. 2022YFA1203100).

ORCID iD

Xiaobing Luo https://orcid.org/0000-0002-6423-9868

References

[1] Mecklenburg M, Mizushima D, Ohtake N, Bauhofer W, Fiedler B and Schulte K 2015 On the manufacturing and electrical and mechanical properties of ultra-high wt.% fraction aligned MWCNT and randomly oriented CNT epoxy composites *Carbon* **91** 275–90

[2] Anand S, Vu M C, Mani D, Kim J-B, Jeong T-H, Islam A and Kim S-R 2023 Dual 3D networks of graphene derivatives based polydimethylsiloxane composites for electrical insulating electronic packaging materials with outstanding electromagnetic interference shielding and thermal dissipation performances *Chem. Eng. J.* **462** 142017

[3] Huang T Q, Wang T, Jin J, Chen M and Wu L M 2023 Design of silicon rubber/BN film with high through-plane thermal conductivity and ultra-low contact resistance *Chem. Eng. J.* **469** 143874

[4] Li C, Zeng X-L, Tan L-Y, Yao Y-M, Zhu D-L, Sun R, Xu J-B and Wong C-P 2019 Three-dimensional interconnected graphene microsphere as fillers for enhancing thermal conductivity of polymer *Chem. Eng. J.* **368** 79–87

[5] Coleman J N, Khan U, Blau W J and Gun'ko Y K 2006 Small but strong: a review of the mechanical properties of carbon nanotube–polymer composites *Carbon* **44** 1624–52

[6] Zhang X-D, Yang G and Cao B-Y 2022 Bonding-enhanced interfacial thermal transport: mechanisms, materials, and applications *Adv. Mater. Interfaces* **9** 2200078

[7] Peng L Q, Yu H T, Chen C, He Q X, Zhang H, Zhao F L, Qin M M, Feng F Y and Feng W 2023 Tailoring dense, orientation-tunable, and interleavedly structured carbon-based heat dissipation plates *Adv. Sci.* **10** 2205962

[8] Mao D S, Chen J H, Ren L L, Zhang K, Yuen M M F, Zeng X L, Sun R, Xu J-B and Wong C-P 2019 Spherical core-shell Al@Al_2O_3 filled epoxy resin composites as high-performance thermal interface materials *Composies* A **123** 260–9

[9] Kim Y-K, Chung J-Y, Lee J-G, Baek Y-K and Shin P-W 2017 Synergistic effect of spherical Al_2O_3 particles and BN nanoplates on the thermal transport properties of polymer composites *Composies* A **98** 184–91

[10] Oya T, Nomura T, Tsubota M, Okinaka N and Akiyama T 2013 Thermal conductivity enhancement of erythritol as PCM by using graphite and nickel particles *Appl. Therm. Eng.* **61** 825–8

[11] Xie B, Zhao W X, Luo X B and Hu R 2023 Alignment engineering in thermal materials *Mater. Sci. Eng.* R **154** 100738

[12] Lei C X, Xie Z L, Wu K and Fu Q 2021 Controlled vertically aligned structures in polymer composites: natural inspiration, structural processing, and functional application *Adv. Mater.* **33** 2103495

[13] Karthik M, Faik A, Blanco-Rodríguez P, Rodríguez-Aseguinolaza J and D'Aguanno B 2015 Preparation of erythritol-graphite foam phase change composite with enhanced thermal conductivity for thermal energy storage applications *Carbon* **94** 266–76

[14] Zhang X-D, Zhang Z-T, Wang H-Z and Cao B-Y 2023 Thermal interface materials with high thermal conductivity and low young's modulus using a solid-liquid metal codoping strategy *ACS Appl. Mater. Interfaces* **15** 3534–42

[15] Yu Z F, Wei S and Guo J D 2019 Fabrication of aligned carbon-fiber/polymer TIMs using electrostatic flocking method *J. Mater. Sci., Mater. Electron.* **30** 10233–43

[16] Uetani K, Ata S, Tomonoh S, Yamada T, Yumura M and Hata K 2014 Elastomeric thermal interface materials with high through-plane thermal conductivity from carbon fiber fillers vertically aligned by electrostatic flocking *Adv. Mater.* **26** 5857–62
[17] Kargar F, Barani Z, Salgado R, Debnath B, Lewis J S, Aytan E, Lake R K and Balandin A A 2018 Thermal percolation threshold and thermal properties of composites with high loading of graphene and boron nitride fillers *ACS Appl. Mater. Interfaces* **10** 37555–65
[18] Nikzad M, Masood S H and Sbarski I 2011 Thermo-mechanical properties of a highly filled polymeric composites for fused deposition modeling *Mater. Des.* **32** 3448–56
[19] Yuan C, Huang M Y, Cheng Y H and Luo X B 2017 Bonding-induced thermal transport enhancement across a hard/soft material interface using molecular monolayers *Phys. Chem. Chem. Phys.* **19** 7352–8
[20] Majumdar S, Sierra-Suarez J A, Schiffres S N, Ong W-L, Higgs C F III McGaughey A J H and Malen J A 2015 Vibrational mismatch of metal leads controls thermal conductance of self-assembled monolayer junctions *Nano Lett.* **15** 2985–91
[21] Chen J, Huang X Y, Sun B and Jiang P K 2019 Highly thermally conductive yet electrically insulating polymer/boron nitride nanosheets nanocomposite films for improved thermal management capability *ACS Nano* **13** 337–45
[22] Zhang X, Jiang J Y, Shen Z H, Dan Z K, Li M, Lin Y H, Nan C-W, Chen L Q and Shen Y 2018 Polymer nanocomposites with ultrahigh energy density and high discharge efficiency by modulating their nanostructures in three dimensions *Adv. Mater.* **30** 1707269
[23] Yuan C, Duan B, Li L, Xie B, Huang M Y and Luo X B 2015 Thermal conductivity of polymer-based composites with magnetic aligned hexagonal boron nitride platelets *ACS Appl. Mater. Interfaces* **7** 13000–6
[24] Zhang X F, Zhou S L, Xie B, Lan W, Fan Y W, Hu R and Luo X B 2021 Thermal interface materials with sufficiently vertically aligned and interconnected nickel-coated carbon fibers under high filling loads made via preset-magnetic-field method *Compos. Sci. Technol.* **213** 108922
[25] Zhang X, Wu K, Liu Y H, Yu B W, Zhang Q, Chen F and Fu Q 2019 Preparation of highly thermally conductive but electrically insulating composites by constructing a segregated double network in polymer composites *Compos. Sci. Technol.* **175** 135–42
[26] Xie K, Liu Y H, Tian Y X, Wu X N, Wu L Y, Mo Y L, Sui G, Du R N, Fu Q and Chen F 2021 Improving the flexibility of graphene nanosheets films by using aramid nanofiber framework *Composies* A **142** 106265
[27] Zhang X F, Xie B, Zhou S L, Yang X, Fan Y W, Hu R and Luo X B 2022 Radially oriented functional thermal materials prepared by flow field-driven self-assembly strategy *Nano Energy* **104** 107986
[28] Zhang J *et al* 2017 A facile method to prepare flexible boron nitride/poly(vinyl alcohol) composites with enhanced thermal conductivity *Compos. Sci. Technol.* **149** 41–47
[29] Zeng X L, Yao Y M, Gong Z Y, Wang F F, Sun R, Xu J B and Wong C-P 2015 Ice-templated assembly strategy to construct 3D boron nitride nanosheet networks in polymer composites for thermal conductivity improvement *Small* **11** 6205–13
[30] Wang C H, Chen X, Wang B, Huang M, Wang B, Jiang Y and Ruoff R S 2018 Freeze-casting produces a graphene oxide aerogel with a radial and centrosymmetric structure *ACS Nano* **12** 5816–25
[31] Liu D Y, Lei C X, Wu K and Fu Q 2020 A multidirectionally thermoconductive phase change material enables high and durable electricity *via* real-environment solar-thermal-electric conversion *ACS Nano* **14** 15738–47
[32] Xie B, Wang Y J, Liu H C, Ma J L, Zhou S L, Yu X J, Lan W, Wang K, Hu R and Luo X B 2022 Targeting cooling for quantum dots by 57.3 °C with air-bubbles-assembled three-dimensional hexagonal boron nitride heat dissipation networks *Chem. Eng. J.* **427** 130958
[33] Erb R M, Libanori R, Rothfuchs N and Studart A R 2012 Composites reinforced in three dimensions by using low magnetic fields *Science* **335** 199–204
[34] Moore A L and Shi L 2014 Emerging challenges and materials for thermal management of electronics *Mater. Today* **17** 163–74
[35] Li J C, Li F Z, Zhao X Y, Zhang W F, Li S J, Lu Y L and Zhang L Q 2020 Jelly-inspired construction of the three-dimensional interconnected BN network for lightweight, thermally conductive, and electrically insulating rubber composites *ACS Appl. Electron. Mater.* **2** 1661–9
[36] Kokkinis D, Schaffner M and Studart A R 2015 Multimaterial magnetically assisted 3D printing of composite materials *Nat. Commun.* **6** 8643
[37] Compton B G and Lewis J A 2014 3D-printing of lightweight cellular composites *Adv. Mater.* **26** 5930–5
[38] Cho D, Choi Y, Park J K, Lee J, Yoon B I and Lim Y S 2004 Thermal conductivity and thermal expansion behavior of pseudo-unidirectional and 2-directional quasi-carbon fiber/phenolic composites *Fibers Polym.* **5** 31–38
[39] Lalet G, Kurita H, Heintz J-M, Lacombe G, Kawasaki A and Silvain J-F 2014 Thermal expansion coefficient and thermal fatigue of discontinuous carbon fiber-reinforced copper and aluminum matrix composites without interfacial chemical bond *J. Mater. Sci.* **49** 397–402